

Modeling Spatial Nonstationarity via Deformable Convolutions for Deep Traffic Flow Prediction

Wei Zeng, *Member, IEEE*, Chengqiao Lin, Kang Liu,
Juncong Lin, *Member, IEEE*, Anthony K. H. Tung, *Senior Member, IEEE*

Abstract—Deep neural networks are being increasingly used for short-term traffic flow prediction. Existing convolution-based approaches typically partition an underlying territory into grid-like spatial units, and employ standard convolutions to learn spatial dependence among the units. However, standard convolutions with fixed geometric structures cannot fully model the nonstationary characteristics of local traffic flows. To overcome the deficiency, we introduce deformable convolution that augments the spatial sampling locations with additional offsets, to enhance the modeling capability of spatial nonstationarity. On this basis, we design a deep deformable convolutional residual network, namely *DeFlow-Net*, that can effectively model global spatial dependence, local spatial nonstationarity, and temporal periodicity of traffic flows. Furthermore, to fit better with convolutions, we suggest to first aggregate traffic flows according to pre-conceived regions of interest, then dispose to sequentially organized raster images for network input. Extensive experiments on real-world traffic flows demonstrate that *DeFlow-Net* outperforms existing solutions using standard convolutions, and spatial partition by pre-conceived regions further enhances the performance. Finally, we demonstrate the advantage of *DeFlow-Net* in maintaining spatial autocorrelation, and reveal the impacts of partition shapes and scales on deep traffic flow prediction.

Index Terms—Traffic flow prediction, spatial nonstationarity, deformable convolution, deep learning

1 INTRODUCTION

TRAFFIC flow prediction should yield accurate projections on the expected traffic conditions, in order to support intelligent transportation systems [30]. Numerous data-driven approaches, such as auto regressive integrated moving average (ARIMA) and its variants (e.g., [22], [33]) that take advantages of repeating occurrences in temporal historical traffic data, have been developed for traffic flow prediction. However, it is a challenging task for conventional approaches to model the complex non-linear spatial and temporal patterns of traffic flows. Recently, research focus has shifted towards utilizing deep neural networks (DNNs) for traffic flow prediction. Many DNN-based solutions have been developed, including residual convolution-based and graph-based neural networks, and achieve superior performances than conventional approaches.

Among them, convolution-based approaches typically partition an underlying territory into grid-like regions, and aggregate in- and out-flows in each region. In this way, traffic flows are represented in raster image format, which is consumable by convolutions. Next, standard convolutions are employed to learn the spatial dependence of traffic flows at pairs of locations. Standard convolution has shown to be effective, since traffic flows observed at a spatial unit are dependent on traffic flows at nearby spatial units, i.e., *spatial dependence* [29]. In a context of urban environments,

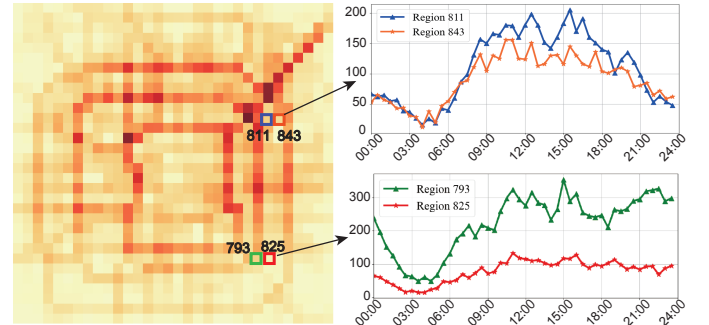


Fig. 1. Traffic flows intrinsically feature locally spatial nonstationarity between sets of neighboring regions. Traffic flows of regions 811 & 843 show similar temporal variations (right-top), whilst those of regions 793 & 825 are distinct (right-bottom).

traffic flows of people movements are highly associated with the functionality of a place [38], [40]. For example, two residences may show similar periodic patterns, e.g., large out-flows in the morning and in-flows in the evening on weekdays. In contrast, daily pendulum movements can be observed between residential and official places [41].

Besides spatial dependence, traffic flows also feature locally *spatial nonstationarity* that depicts varying relationships between some sets of variables over space [3]. Fig. 1 (left) presents traffic flows in Beijing that is divided into 32×32 grid regions. Two sets of neighboring regions are selected: 1) regions 811 & 843, and 2) regions 793 & 825. Temporal variations of averaged traffic flows of these regions are presented in Fig. 1 (right). Here, regions 811 & 843 show similar flow dynamics, whilst those of regions 793 & 825 are different. Standard convolution with a fixed geometric structure (e.g., a 3×3 kernel) cannot capture the varying relationships between the two sets of regions, not to mention

- W. Zeng and K. Liu are with Shenzhen Institutes of Advanced Technology, Chinese Academy of Sciences. e-mail: {wei.zeng, kang.liu}@siat.ac.cn.
- C. Lin and J. Lin (corresponding author) are with Xiamen University, China. E-mail: {linchengqiao, jclin}@xmu.edu.cn.
- A.K.H. Tung is with School of Computing, National University of Singapore. E-mail: atung@comp.nus.edu.sg.

Manuscript received xx xx, 202x; revised xx xx, 202x.

if we consider sets of over two regions. As such, existing convolution-based approaches are incompetent to model spatial nonstationarity of traffic flows.

This paper tackles the problems with a feasible solution from two perspectives. First, we observe that most of existing convolution-based approaches for traffic flow prediction partition the underlying territory into grid regions. The partition scheme however increases spatial nonstationarity, and consequently harms prediction performance of the network. To mitigate the issue, we suggest to aggregate traffic flows according to pre-conceived regions of interest (RoIs), e.g., traffic analysis zones (TAZs) or functional regions. The aggregated traffic flows are passed through a rasterization process and disposed to raster images. Second, we propose to advocate the use of deformable convolution [9], which has shown to be effective for many applications, such as semantic image segmentation [5] and image deblurring [39]. Specifically, deformable convolution augments the spatial sampling locations with additional offsets, and learns the offsets from the spatial distributions of traffic flows. In this way, deformable convolution not only inherits the ability of standard convolution in learning spatial dependence, but also being able to alter over space to capture the nonstationary characteristics of traffic flows.

On these basis, we design *DeFlow-Net*, which is a deformable convolutional residual network for accurate short-term traffic flow prediction. Besides deformable convolutions for modeling spatial dependence and nonstationarity, *DeFlow-Net* also incorporates a temporal dependency module to learn temporal patterns of traffic flows from weekly trend, daily periodicity, and hourly closeness components. The temporal feature components are fused together to predict the future trend. We conduct extensive experiments on real-world traffic flows in Beijing, New York City, and Shenzhen. The results demonstrate that *DeFlow-Net* outperforms existing convolution-based methods for traffic flow prediction, and ablated techniques with standard and atrous convolutions, in terms of both prediction accuracy and the ability to maintain spatial autocorrelation. The study further reveals that spatial partition by pre-conceived regions also contributes to performance improvements.

The main contributions of this work include:

- We design *DeFlow-Net*, a deep deformable convolutional residual network that takes advantages of deformable convolutions to model both spatial dependence and nonstationarity (Sect. 3.2).
- We evaluate the effectiveness of *DeFlow-Net* on real-world traffic flows in three cities, and compare with baseline models and ablated techniques. The comparison results indicate our proposed model outperforms existing methods in terms of both prediction accuracy (Sect. 4.3) and the ability to preserve spatial autocorrelation (Sect. 4.4).
- We conduct local indicators of spatial autocorrelation (LISA) analysis [1], and reveal the impacts of partition shapes and scales on predictions (Sect. 4.5). The study confirms the effectiveness of integrating RoIs when preparing network inputs (Sect. 3.1).

TABLE 1
Meanings of all notations.

SYMBOL	DESCRIPTION
$\mathcal{M}; m$	all movements; a movement.
$\mathcal{T}; t$	all time slots; a time slot.
$\mathcal{R}; r$	all regions; a region.
$X_{\mathcal{R},t}; x_{r,t}$	in-/out-flow of regions \mathcal{R} at time slot t ; in-/out-flow of a region r at time slot t .
$G; g$	grid map; a grid.
$X_{G,t}; x_{g,t}$	in-/out-flow of grid map G at time slot t ; in-/out-flow of a grid g at time slot t .
$Y_{G,t}; y_{g,t}$	predicted in-/out-flow of grid map G at time slot t ; predicted in-/out-flow of a grid g at time slot t .

2 PROBLEM DEFINITION

This section introduces fundamental concepts of our work. Table 1 lists down the notations used throughout the paper. The input data in our problem is a set of movements \mathcal{M} that denotes the mobility of multiple moving objects (e.g., mobile users and taxi cabs) throughout a time period \mathcal{T} . We divide \mathcal{T} into equal-time slots to analyze the movements in time-series discretely, i.e., $\mathcal{T} := \{t_1, \dots, t_n\}$.

Definition 1 (Movement). A movement m is a continuously measured trajectory of a moving object during a time period \mathcal{T} , which is defined by a set of spatiotemporal records $\bigcup_{t \in \mathcal{T}} \langle t, l_t \rangle$, where l_t represents the position of m at time t . We denote all movements of multiple moving objects as \mathcal{M} .

Definition 2 (Region). We partition an underlying territory into a set of regions \mathcal{R} that are non-overlapping and fill-up the territory. Each region r can be 1) a grid partitioned based on the longitude and latitude, or 2) pre-conceived region of interest (RoI), e.g., a functional zone isolated by road network, or a TAZ constructed by census block information for tabulating traffic-related data. RoIs are typically in irregular shapes.

From the movements \mathcal{M} , we compute inflow $x_{r,t}^I$ and outflow $x_{r,t}^O$ per time slot t for each region $r \in \mathcal{R}$.

Definition 3 (Inflow & Outflow). We define the inflow $x_{r,t}^I$ of a region r at time slot t as the number of moving objects who are not in r at time slot $t-1$ and appear in r at time slot t , i.e.,

$$x_{r,t}^I = |\{m \in \mathcal{M} | m.l_{t-1} \notin r \wedge m.l_t \in r\}|, \quad (1)$$

where $|\cdot|$ denotes the cardinality of the set. Similarly, we can compute the outflow $x_{r,t}^O$ as

$$x_{r,t}^O = |\{m \in \mathcal{M} | m.l_{t-1} \in r \wedge m.l_t \notin r\}|. \quad (2)$$

For simplicity, we omit the notations I/O in the following. The simplified symbols represent either inflow or outflow, unless specified. We compute in/out traffic flows for all regions $r \in \mathcal{R}$ at all time slots $t \in \mathcal{T}$, yielding a series of traffic flows $\{X_{\mathcal{R},t} | t \in \mathcal{T}\}$.

Problem Definition (Short-Term Traffic Flow Prediction). Consider a set of movements \mathcal{M} in the time duration of \mathcal{T} , a set of regions \mathcal{R} , and a series of derived traffic flows $\{X_{\mathcal{R},t} | t \in \mathcal{T}\}$, our goal is to predict unobserved traffic flows $Y_{\mathcal{R},t_{n+1}}$ for \mathcal{R} at time slot t_{n+1} . Accuracy is of primary concern for short-term traffic flow prediction, i.e., output predictions shall be close to ground truths. In addition, this work

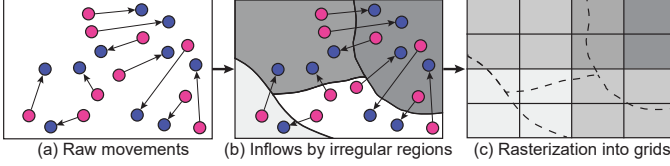


Fig. 2. A general pipeline of creating gridded traffic flows as network inputs: Raw movements (a) are counted as inflows based on irregular regions (b), and further rasterized into a grid map (c).

also considers *spatial autocorrelation* as a key performance indicator, as spatial units of locally high nonstationarity are more likely to produce high prediction errors [42].

3 METHODOLOGY

We propose to tackle the problem from two perspectives. First, we introduce a preprocessing procedure that integrates pre-conceived RoIs when preparing network consumable inputs (Sect. 3.1). Next, we present *DeFlow-Net*, a deep deformable convolutional residual neural network built upon deformable convolutions (Sect. 3.2). The training scheme for *DeFlow-Net* is described in Sect. 3.3.

3.1 Integrating RoIs and Movements

As discussed in Definition 2, this work considers both grid partitions based on the longitude and latitude, and partitions by irregular RoIs such as TAZs. The two alternative partition approaches can generate different traffic flows, as statistical measurements are subject to the boundaries of spatial units, *i.e.*, the *modifiable areal unit problem* (MAUP) [13], [25]. In addition, studies have shown that deep neural networks generally suffer from the adversarial perturbation problem [23], [46]. As such, the network predictions of traffic flows can be significantly different, even if the input difference is marginal. However, most of existing convolution-based traffic prediction methods only explore grid partitions based on the longitude and latitude, *e.g.*, [43], [37], whilst neglect partitions by RoIs. This work fills the gap and examines the impacts of different partition methods on convolution-based network predictions.

Using RoIs in irregular shapes, the generated in/out traffic flows $X_{\mathcal{R},t}$ show non-grid-like topology. However, a convolution operation needs inputs to be in raster-image format which can be processed by the receptive field. As such, we first convert $X_{\mathcal{R},t}$ into a raster image $X_{G,t} \in \mathbb{R}^{i \times j}$. The process is denoted as *rasterization*, as illustrated in Fig. 2.

Definition 4 (Rasterization). We divide the underlying territory into a grid map G of size $i \times j$ (*e.g.*, 4×4 as in Fig. 2). Each grid $g \in G$ can intersect with arbitrary number of irregular regions $\{r_k\}_{k=1}^n$. We calculate the in/out traffic flow for each grid g at time slot t as:

$$x_{g,t} = \sum_{k=1}^n x_{r_k,t} \times \frac{S(r_k \cap g)}{S(r_k)}, \quad (3)$$

where $S(\cdot)$ stands for the area of a region, and $r_k \cap g$ indicates the intersection between r_k and g .

In this way, we construct a raster image $X_{G,t} \in \mathbb{R}^{i \times j}$ that represents the in/out traffic flows of the grid map G . We perform the rasterization process for all time slots $t \in \mathcal{T}$,

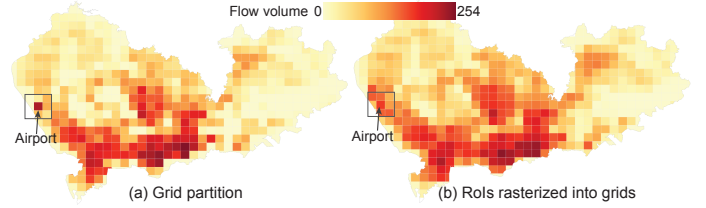


Fig. 3. Comparison of traffic flows in Shenzhen by grid partition based on the longitude and latitude (left), and by RoI partition followed by rasterization (right). Both raster images are the size of 50×25 .

yielding a series of raster images $\{X_{G,t} \in \mathbb{R}^{i \times j} | t \in \mathcal{T}\}$. Fig. 3 presents a comparison of traffic flows in Shenzhen by the two partition alternatives. In Fig. 3(a), the traffic flows are aggregated using a 50×25 grid map based on the longitude and latitude. In Fig. 3(b), the traffic flows are first aggregated based on RoIs (here 491 TAZs in Shenzhen), and then rasterized based on a grid map of the same resolution 50×25 . There are noticeable differences between the two raster images. Especially in the airport area, grid partition produces an extreme high volume for the grid in the center, whilst the grid has similar flow volume with those surrounding grids in RoI partition. The reason is that the TAZ where locates the airport is big, and the traffic flows are averaged by grids intersecting with the TAZ. The input differences have a significant impact on prediction accuracy of the outputs, as we will show in the experiment.

3.2 DeFlow-Net

Overview. We design *DeFlow-Net* that takes a series of raster images $\{X_{G,t} \in \mathbb{R}^{i \times j} | t \in \mathcal{T}\}$ as inputs, and predicts traffic flows $Y_{G,t_{n+1}}$ for the grid map G at time slot t_{n+1} . The predicted traffic flow $Y_{G,t_{n+1}}$ can be expressed as:

$$Y_{G,t_{n+1}} = \mathcal{F}_\theta(\{X_{G,t_1}, X_{G,t_2}, \dots, X_{G,t_n}\}), \quad (4)$$

where $\mathcal{F}_\theta(\cdot)$ represents the proposed *DeFlow-Net* model, while θ are the learnable parameters. Fig. 4 presents the overall framework of *DeFlow-Net*, which is composed of the following modules:

- *Temporal Dependency Module* (Sect. 3.2.1). The module models the periodic patterns of traffic flows using temporal components of weekly trend, daily periodicity, and hourly closeness.
- *Deformable Convolution Module* (Sect. 3.2.2). The module learns spatial dependence and nonstationarity using deformable convolutions, and deepens the convolutional layers using residual unit.
- *Fusion and Activation Module* (Sect. 3.2.3). Last, *DeFlow-Net* fuses the three temporal components to model spatial-temporal correlation, and activates the final prediction.

3.2.1 Temporal Dependency Module

Traffic flows in historical data feature periodic patterns. Most of the studies on short-term traffic flow predictions, including deep-learning-based approaches (*e.g.*, [43], [16]), make use of this property. Following previous conventions, *DeFlow-Net* employs three components of weekly trend that associates distant time slots in one-week, daily periodicity

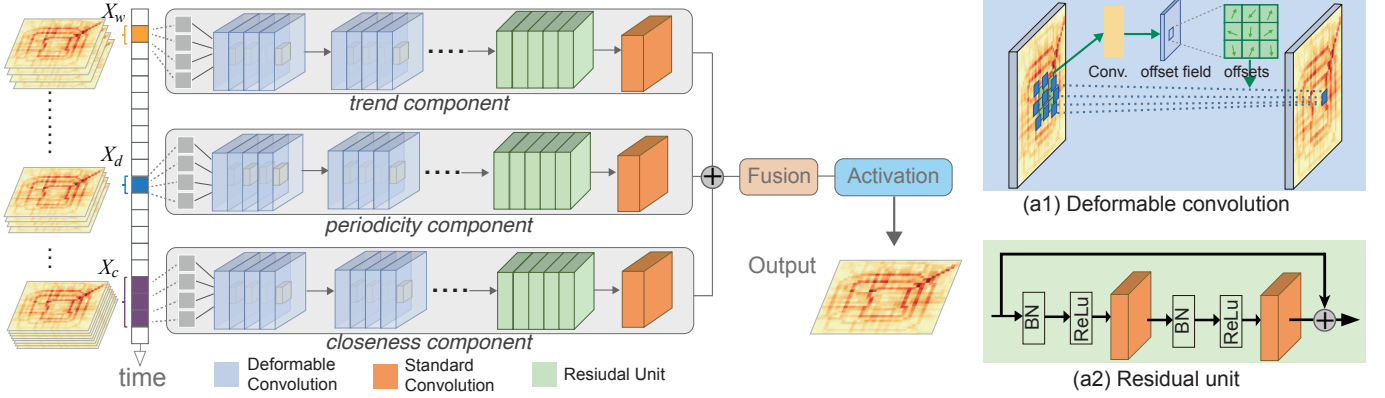


Fig. 4. Network architecture of our *DeFlow-Net*, which mainly consists of three modules: (i) a *temporal dependency module* including weekly *trend*, daily *periodicity*, and hourly *closeness* components to learn periodic patterns; (ii) a *deformable convolution module* taking advantage of deformable convolutions (b1) to learn spatial dependence, and residual units (b2) to increase network depth; and (iii) a *fusion and activation module* to fuse temporal components and activate the final prediction.

that associates near time slots in one-day, and hourly *closeness* that associates recent time slots in a few hours, to model temporal dependency.

Inputs for weekly trend component are a subsequence of raster images from the previous week. We can define the weekly trend component as $[X_{G,t-\Delta w \cdot p_w}, X_{G,t-(\Delta w-1) \cdot p_w}, \dots, X_{G,t-p_w}]$, where Δw represents length of the raster image subsequence from the previous weeks, and p_w is fixed to one-week length, i.e., $p_w = 48 \times 7$. Similarly, we define daily trend component as $[X_{G,t-\Delta d \cdot p_d}, X_{G,t-(\Delta d-1) \cdot p_d}, \dots, X_{G,t-p_d}]$, where Δd represents length of the raster image subsequence from the previous days, and p_d is fixed to one-day length, i.e., $p_d = 48$. In the closeness component, we select the previous Δc time slots of traffic flows to infer the next time slot. Hence, the closeness component is defined as $[X_{G,t-\Delta c}, X_{G,t-(\Delta c-1)}, \dots, X_{G,t-1}]$.

3.2.2 Deformable Convolution Module

Traffic flows that measure continuous movements across spatial units are by nature spatially dependent. For instance, regions with similar functionality [38] or POI distributions [40] are likely to show similar traffic flows as well. We utilize a *Deformable Convolution Module* to model spatial dependence among traffic flows.

Inputs of the module are *trend*, *periodicity*, and *closeness* components from the *Temporal Dependency Module*. We first concatenate the sequential raster images in each component as one tensor. Taking the *closeness* component for example, we concatenate both inflow and outflow raster images $[X_{G,t-\Delta c}, X_{G,t-(\Delta c-1)}, \dots, X_{G,t-1}]$ together, yielding $X_{G,c}^{(1)} \in \mathcal{R}^{2\Delta c \times i \times j}$ (notation $^{(1)}$ indicates input for the first convolutional layer). $X_{G,c}^{(1)}$ is then fed into multiple convolutional layers. The transformation matrix for the l -th convolutional layer can be defined as:

$$X_{G,c}^{(l+1)} = f_c(W_{G,c}^{(l)} * X_{G,c}^{(l)} + b_{G,c}^{(l)}), \quad (5)$$

where $*$ denotes the convolution operation, while $W_{G,c}^{(l)}$ and $b_{G,c}^{(l)}$ are two sets of learnable parameters in the k -th convolution layer. $f_c(\cdot)$ is the activation function, for which we use the rectified linear unit (ReLU), i.e., $f_c(z) = \max(0, z)$.

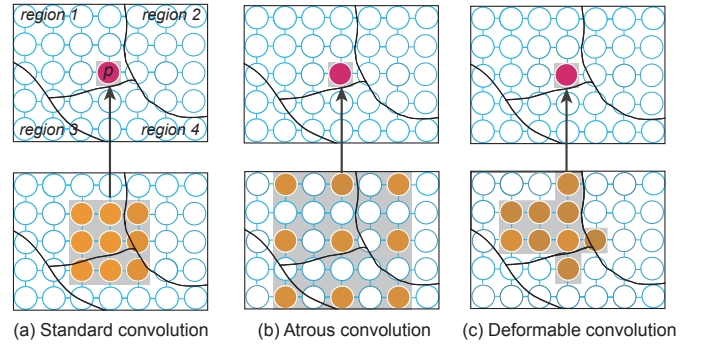


Fig. 5. Illustration of the convolution alternatives. Left to right: (a) the receptive field of a standard convolution covers grids from different regions; (b) atrous convolution (atrous rate $r = 2$) enlarges the receptive field but the grids are also from different regions; (c) deformable convolution covers neighboring grids or grids in the same region.

To ensure the input and output have the same size, we use zero paddings for grids at the boundary.

Convolutional Layers. Convolution is applied to make use of the spatial relationship among nearby grids covered by the receptive field. Intuitively, convolutions can learn spatial dependence because traffic flows in neighboring regions can affect each other. There are three convolution alternatives (see Fig. 5) that can lead to different effects:

- **Standard convolution.** Consider a location \mathbf{p} (red unit in the top row of Fig. 5) in $X_{G,c}^{(l+1)}$, a standard convolution can be defined as:

$$X_{G,c}^{(l+1)}[\mathbf{p}] = \sum_{\mathbf{k} \in \mathcal{K}} W_{G,c}^{(l)}[\mathbf{k}] * X_{G,c}^{(l)}[\mathbf{p} + \mathbf{k}], \quad (6)$$

where $X_{G,c}^{(l)}[\mathbf{p} + \mathbf{k}]$ represents pixel at the position $\mathbf{p} + \mathbf{k}$ in $X_{G,c}^{(l)}$, and \mathbf{k} is the location offset in \mathcal{K} . For a kernel of the size 3×3 , \mathcal{K} is defined as:

$$\mathcal{K} = \{(-1, -1), (-1, 0), \dots, (0, 1), (1, 1)\}. \quad (7)$$

Standard convolution is commonly adopted in many CNN architectures. However, standard convolution may not be optimal for learning spatial dependence in short-term traffic prediction. As shown in Fig. 5(a), the unit marked in red is in region 1, whilst the

receptive field of a standard convolution covers units distributed in 4 different regions. If the regions have different functionalities, spatial dependence of traffic flows among these units would be low, causing weak feature representation.

- **Atrous convolution.** Atrous convolution enlarges a convolution's field-of-view by inserting holes between pixels, to capture objects at multiple scales. Atrous convolution can be defined as:

$$X_{G,c}^{(l+1)}[\mathbf{p}] = \sum_{\mathbf{k} \in \mathcal{K}} W_{G,c}^{(l)}[\mathbf{k}] * X_{G,c}^{(l)}[\mathbf{p} + r \times \mathbf{k}], \quad (8)$$

where r is the atrous rate that specifies $r - 1$ zeros along each spatial dimension. In case that $r = 1$, atrous convolution is equivalent to standard convolution. As such, atrous convolution can be regarded as a general form of standard convolution.

Atrous convolution can improve the feature capturing capability with a large atrous convolution, as shown in Fig. 5(b). However, the receptive field is still symmetric, forcing the convolutional layer to learn spatial dependence in symmetric units. In contrast, regions are typically in irregular shapes. In this sense, atrous convolution may even worsen the feature representation of spatial dependence, as it learns from distant regions [29].

- **Deformable convolution.** The deficiency of standard and atrous convolutions also applies to image segmentation of segmenting an image into multiple segments in regular shapes. Deformable convolution is proposed to address the deficiency, by introducing additional 2D offsets to the receptive field [9]. A deformable convolution can be expressed as:

$$X_{G,c}^{(l+1)}[\mathbf{p}] = \sum_{\mathbf{k} \in \mathcal{K}} W_{G,c}^{(l)}[\mathbf{k}] * X_{G,c}^{(l)}[\mathbf{p} + \mathbf{k} + \Delta\mathbf{k}], \quad (9)$$

where $\Delta\mathbf{k}$ is the offset applied to the location offset \mathbf{k} . Fig. 5(c) shows an illustration of a deformable convolution applied to traffic flows. Here, the receptive field overlaps much with region 1, where \mathbf{p} is located. The other two sampling units are outside region 1, but they are neighbors of \mathbf{p} . That is, the deformable convolution effectively learns spatial dependence from neighboring units, or those located in the same region with \mathbf{p} .

As shown in Fig. 4(b), the offset $\Delta\mathbf{k}$ is obtained through a convolutional layer appended after a standard convolution layer. In this way, *DeFlow-Net* can realize the standard back-propagation for end-to-end training. It is worth noting that learnable parameters $\Delta\mathbf{k}$ are mostly fractional. We complete the convolution by bilinear interpolation, in order to obtain the values at the fractional positions.

Residual Unit. Nevertheless, one convolutional layer can only account for dependence in nearby regions, due to the limited size of kernels. To further enrich the spatial dependence between distant regions, *DeFlow-Net* utilizes multiple deformable convolutional layers. However, error

back propagation becomes more difficult as the number of layers increases, causing the model degradation and vanishing gradient problems. Residual network [17] is introduced to address the problem, by utilizing shortcut connections achieved with batch normalization, ReLU activation, and standard convolution, as illustrated in Fig. 4(c). The residual unit can be expressed as:

$$X_{G,c}^{(l+1)} = X_{G,c}^{(l)} + \mathcal{F}_r \left(X_{G,c}^{(l)}, W_{G,c}^{(l)} \right), \quad (10)$$

where $\mathcal{F}_r(\cdot)$ denotes the residual function, and $W_{G,c}^{(l)}$ is the weight matrix set associated with the residual unit that needs to be learned. Note here standard convolution is adopted instead of deformable convolution to reduce computational cost. Prediction performance is not affected since spatial nonstationarity has been learned by deformable convolutional layers already.

Finally, we fuse the feature maps in each component through a standard convolution.

3.2.3 Fusion and Activation Module

After multiple convolutional layers and residual units in the *Deformable Convolution Module*, we derive $X'_{G,c}$ for the *closeness* component. Similarly, we derive $X'_{G,d}$ and $X'_{G,w}$ for the *periodicity* and *trend* components, respectively. Next, *DeFlow-Net* employs a fusion layer to fuse the three components together, to simultaneously model the spatial and temporal correlations. The fusion layer can be expressed as:

$$X_G^{Fusion} = W_c \circ X'_{G,c} + W_d \circ X'_{G,d} + W_w \circ X'_{G,w}, \quad (11)$$

where W_c , W_d , and W_w are learnable parameters that adjust the degrees of *closeness*, *periodicity*, and *trend* components, respectively. We use the Hadamard product for \circ , which produces the sum of element-wise multiplication of two matrices. Last, we employ an active function to predict traffic flow $Y_{G,t_{n+1}}$ at time slot $t + 1$ for the grid map G . The activation can be expressed as:

$$Y_{G,t_{n+1}} = \tanh(X_G^{Fusion}), \quad (12)$$

where \tanh is a hyperbolic tangent that ensures the output values are between -1 and 1.

3.3 Training Scheme

We normalize the training data to $[-1, 1]$ using Max-Min normalization on the input datasets. Then, we denormalize the predictions and compare them with the groundtruths. We use the Adam optimizer to minimize mean squared error between the predicted traffic flow $Y_{G,t_{n+1}}$ and the groundtruth $X_{G,t_{n+1}}$:

$$\mathcal{L}(\theta) = \|X_{G,t_{n+1}} - Y_{G,t_{n+1}}\|_2^2, \quad (13)$$

where θ is learnable parameters in our model.

We implement *DeFlow-Net* with Keras that uses TensorFlow as the backend. *DeFlow-Net* can be trained in an end-to-end manner via back-propagation. All kernels of the convolutions are set to 3×3 in size. The parameters for the three temporal components are set as: $\Delta w = 1$, $\Delta d = 1$, and $\Delta c = 3$, which empirically produces good results. The

TABLE 2
Statistics of the datasets used in the experiment.

Dataset	TaxiBJ	BikeNYC	TaxiSZ
Data type	Taxi GPS	Bike rent	Taxi GPS
Location	Beijing	New York	Shenzhen
Time period (days)	528	183	181
Time slot (minutes)	30	60	30
Available time slots	22,459	4,392	8,688
Has RoI?	No	No	491 TAZs
Grid map size	32×32	8×16	50×25 & 100×50

batch size during the training is set to 32 and the learning rate is set to 0.001. In addition, to obtain optimal model parameters and prevent overfitting, we perform the early-stopping strategy during training to control the number of epochs. All experiments were conducted on a server (AMD Ryzen 7 2700 8-Core Processor $\times 16$, NVIDIA GeForce RTX 2080 GPU) with Linux operation system.

4 EXPERIMENT

We conduct extensive experiments to evaluate the effectiveness of our proposed *DeFlow-Net*. This section presents the datasets (Sect. 4.1), baseline models and ablated techniques (Sect. 4.2), and quantitative comparison results (Sect. 4.3). In the end, we further perform spatial autocorrelation analysis (Sect. 4.4), and discuss the impacts of different partition shapes and scales (Sect. 4.5).

4.1 DataSets

We use three real-world datasets to evaluate the performance of our model: TaxiBJ, BikeNYC, and TaxiSZ. Statistics of the datasets are summarized in Table 2, and the details are described as follows:

- **TaxiBJ:** *TaxiBJ* records taxicab GPS data in Beijing, during four periods from 1st Jul. 2013 to 30th Oct. 2013, 1st Mar. 2014 to 30th Jun. 2014, 1st Mar. 2015 to 30th Jun. 2015, and 1st Nov. 2015 to 10th Apr. 2016. There are in total 528-day records divided into 30-minute time slots, yielding a total of 22,459 time slots (some slots are omitted due to corrupted data). The city of Beijing is divided into a 32×32 grid map according to the longitude and latitude. The data from the last four weeks are used for testing, while the rest are used for training.
- **BikeNYC:** *BikeNYC* records bike trajectories taken from the the NYC Bike System, from 1st Apr. 2014 to 30th Sept. 2014. There are in total 183-days records divided into 60-minute tile slots, yielding a total of 4,392 time slots. BikeNYC is organized in a grid map of scale 8×16 . We take the last ten days data for testing, and the rest for training.
- **TaxiSZ:** *TaxiSZ* records taxi transactions carried out by over 20k taxis during the period from 1st Jan. 2019 to 30th Jun. 2019. Unlike publicly available *TaxiBJ* and *BikeNYC* that have been cleaned up and preprocessed, *TaxiSZ* contains approximately 800k raw transaction records per day, making a total of over 145 million transaction records in 181 days. The

raw data include numerous corrupted or incomplete information, such as positions outside Shenzhen or missing get-on/-off times. We clean up the data by removing these records, yielding about 128 million transaction records ready for use. Next, we divide the data into 30-minute time slots, resulting in a total of 8,688 time slots. We use the data from the last two weeks for testing, and the rest for training.

Besides, we also have 491 TAZs that are designated by the transportation department in Shenzhen for tabulating traffic-related census data. The TAZ borders correspond well with recognizable physical boundaries, such as main streets and waters. In this way, the land use and activities within each TAZ are relatively homogeneous. We use the TAZ information to evaluate the benefits of RoI partition.

4.2 Baselines and Ablations

To evaluate the effectiveness of *DeFlow-Net*, we first compare with four baseline models as follows:

- **HA:** Historical Average (HA) uses historical average traffic flows of a given region at the corresponding time. We average traffic flows of the last three week to make the estimation.
- **ARIMA:** Auto-Regressive Integrated Moving Average (ARIMA) is a well-known method for predicting future trends of a time series. ARIMA has been widely used in traffic flow prediction.
- **ST-ResNet [43]:** ST-ResNet is one of the first convolution-based deep traffic flow prediction models. ST-ResNet can also incorporate external factors such as weather information, which is omitted in the experiment for fair comparison.
- **ST-3DNet [16]:** ST-3DNet exploits a specially designed 3D CNN architecture to learn spatial and temporal features in traffic flows simultaneously. It is one of the latest convolution-based deep traffic flow prediction models.

We use the same training scheme for *ST-ResNet* and *ST-3DNet*, including loss function and kernel size, as those in *DeFlow-Net*. Next, we also compare to two ablated techniques that utilize standard convolutions and atrous convolutions, instead of deformable convolutions in *DeFlow-Net*.

- **Standard Convolution:** We use a fixed kernel of 3×3 size to account for adjacency relationships. All other settings are the same with those in *DeFlow-Net*.
- **Atrous Convolution:** We use a 3×3 kernel with an atrous rate of 2. This setting uses 9 parameters, but achieves the same field of view as a 5×5 standard convolution kernel. All other settings are the same with those in *DeFlow-Net*.

Last, we test the impacts of partition shapes and scales on prediction performances. We compare grid and RoI partition for *TaxiSZ*, whilst omit *TaxiBJ* and *BikeNYC* that have been preprocessed using grid partition.

- **TaxiSZ (Grid) 50 \times 25:** We first partition the underlying territory of Shenzhen into 50 \times 25 grids based

TABLE 3
Comparison with baseline models.

Model	TaxiBJ		NYCBike		TaxiSZ	
	RMSE	MASE	RMSE	MASE	RMSE	MASE
HA	52.77	0.605	10.76	0.230	12.41	0.409
ARIMA	28.46	0.672	9.98	0.245	11.37	0.437
ST-ResNet	17.34	0.295	6.48	0.171	6.54	0.395
ST-3DNet	17.14	0.292	5.95	0.168	5.62	0.234
DeFlow-Net	15.90	0.278	5.85	0.165	5.35	0.236

on the longitude and latitude, then aggregate in- and out-flows in each grid.

- **TaxiSZ (Grid) 100×50**: The city is partitioned into 100×50 grids for aggregation of in- and out-flows.
- **TaxiSZ (RoI) 50×25**: We first aggregate traffic flows in each of the 491 TAZs, followed by a rasterization process using 50×25 grid map.
- **TaxiSZ (RoI) 100×50**: The rasterization is performed upon a 100×50 grid map after aggregation.

We train a *DeFlow-Net* model for each of these *TaxiSZ* variants. We abbreviate *TaxiSZ (Grid) 50×25* as *TaxiSZ*, which is of similar size with *TaxiBJ*, when comparing to baseline models and ablated techniques.

4.3 Performance Comparison

Evaluation Metrics: To evaluate and compare the performance of different models, we first adopt root mean square error (RMSE) as in previous studies.

$$RMSE = \sqrt{\frac{1}{N} \sum_{g=1}^N (x_{g,t_{n+1}} - y_{g,t_{n+1}})^2}, \quad (14)$$

where N is the number of grids, $x_{g,t_{n+1}}$ and $y_{g,t_{n+1}}$ are the ground truth and predicted traffic flow for grid g at time slot t_{n+1} . However, RMSE measurements are unit dependent, making it unsuitable for comparison between different datasets. To address the problem, we further incorporate mean absolute scaled error (MASE) [19].

$$MASE = \frac{\frac{1}{N} \sum_{g=1}^N |x_{g,t_{n+1}} - y_{g,t_{n+1}}|}{\frac{1}{T-m} \sum_{g=1}^N \sum_{t=m+1}^T |x_{g,t} - x_{g,t-m}|}, \quad (15)$$

where $x_{g,t_{n+1}}$ and $y_{g,t_{n+1}}$ in the numerator are from the testing data, while $x_{g,t}$ and $x_{g,t-m}$ in the denominator are from the training data, respectively. T is the total number of time slots in the training data, and m is the seasonality of the time series (*i.e.*, 48 for *TaxiBJ* and *TaxiSZ*, and 24 for *BikeNYC*). MASE is unit independent, allowing us to compare traffic flow predictions in different cities and at different scales. Moreover, MASE can handle actual values of zero and is not biased by very extreme values, which are problematic for mean absolute percentage error (MAPE) [19]. In general, a MASE less than 1 indicates a model is better than the naive model, and lower MASE indicates better model.

4.3.1 Comparison with Baselines

Experimental results of comparison with baseline models are shown in Table 3. The best performance for each dataset is marked in bold. Here, conventional time-series models, *i.e.*, *HA* and *ARIMA*, produce large RMSEs and MASEs.

TABLE 4
Comparison with ablated techniques of different convolutions.

Convolution	TaxiBJ		BikeNYC		TaxiSZ	
	RMSE	MASE	RMSE	MASE	RMSE	MASE
Standard	17.34	0.295	6.48	0.171	6.54	0.395
Atrous	17.22	0.295	6.16	0.175	5.79	0.477
Deformable	15.90	0.278	5.85	0.165	5.35	0.236

This is probably because *HA* and *ARIMA* only make use of periodic patterns in temporal dimension, whilst deep-learning-based techniques further take advantages of spatial dependence. Among the baselines (*ST-ResNet* and *ST-3DNet*), *ST-3DNet* always achieves better performances for all datasets. The result indicates that 3D convolutions can better learn spatial and temporal features, in comparison with 2D convolutions used in *ST-ResNet*. On the other hand, our *DeFlow-Net* is also based on 2D convolutions, but still achieves better performances in terms of RMSE and MASE for all experimental datasets. Specifically, our model reduces RMSEs to 15.90, 5.85, 5.35, and MASEs to 0.278, 0.165, 0.236, for *TaxiBJ*, *NYCBike*, and *TaxiSZ* respectively. That is, *DeFlow-Net* achieves on average 4.59% RMSE and 1.91% MASE improvements, in comparison with *ST-3DNet*. The result confirms the effectiveness of deformable convolutions that are employed in *DeFlow-Net*, in modeling spatial characteristics of historical traffic flows.

4.3.2 Comparison with Ablated Techniques

Table 4 presents the comparison results of ablated techniques using standard and atrous convolutions. We can notice that the ablation with atrous convolutions performs better in RMSE than the one with standard convolutions on all three datasets. This is probably because atrous convolutions have a larger receptive field, allowing the ablation to better capture multi-scale spatial contextual information. Yet the improvements in terms of MASE is marginal. This indicates that the fixed geometric structure utilized by atrous convolutions, still limits its capability in modeling spatial nonstationarity of local traffic flows. Our model with deformable convolutions achieves better performances on all datasets. Notice that the improvements on different datasets are slightly different. In details, our model with deformable convolutions reduces RMSE by 7.99%, 5.03%, 7.60%, and reduces MASE by 5.76%, 3.51%, 40.25% than the ablation with atrous convolutions, for *TaxiBJ*, *BikeNYC*, and *TaxiSZ*, respectively. The improvements on *TaxiBJ* and *TaxiSZ* datasets are more significant. A possible reason is that the sizes of *TaxiBJ* and *TaxiSZ* grid maps are bigger, leaving more space for the model to learn sampling offsets.

4.4 Spatial Autocorrelation Analysis

Spatial autocorrelation is an important term in spatial statistics, which describes variation of a variable within geographic space. Positive spatial autocorrelation indicates the tendency for locations that are close together to have similar values. There exist many indicators for spatial autocorrelation analysis, such as *Moran's I* [24] and *Geary's C* [12]. Both metrics are one single numeric statistic for measuring global spatial autocorrelation. To quantify local effects that

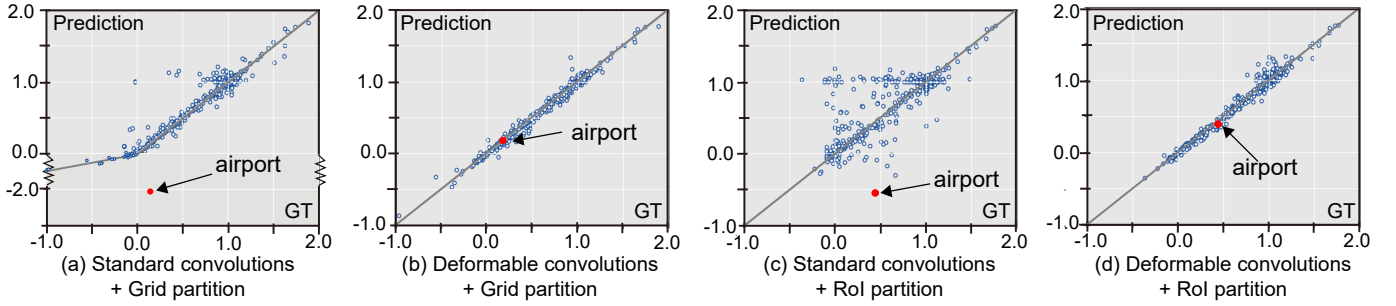


Fig. 6. Q-Q plots of LISA indicators of groundtruth (x-axis) and predicted (y-axis) traffic flows by different combinations of spatial partition shapes and convolution types. Deformable convolutions can better preserve spatial autocorrelation, as the points in (b) & (d) fall close to the diagonal line, whilst many points in (a) & (c) are far distributed from the diagonal line.

manifest spatial nonstationarity, this work adopts local indicators of spatial association (LISA) analyses that decompose the global Moran's I statistic to local Moran's I indices.

Definition 5 (Local Indicators of Spatial Association).

Consider an in-/out-flow matrix $X_{G,t}$, we conduct LISA analysis for a local unit $x_{g_i,t}$ as:

$$I(x_{g_i,t}) = \frac{x_{g_i,t} - \bar{X}_{G,t}}{S^2} \sum_{j=1, j \neq i}^n w_{ij} (x_{g_j,t} - \bar{X}_{G,t}) \quad (16)$$

where $x_{g_i,t}$ indicates flow volume of grid g_i , and $x_{g_j,t}$ is the flow volume of grid g_j that is one neighbor of grid g_i at time slot t . Here, we choose 3×3 surrounding grids as neighbours, corresponding to the size of receptive fields. w_{ij} is an element of spatial weights matrix that measures spatial connectivity between grids g_i and g_j . $\bar{X}_{G,t}$ is the mean flow volume of all grids in G , while S^2 is the variance of flow volumes of neighboring grids.

A positive value of $I(x_{g_i,t})$ indicates that grid g_i has similarly high or low traffic volume as its neighbours, whilst a negative value indicates that g_i is a spatial outlier. We also conduct LISA analyses for the predicted traffic flows in the same way. Fig. 6 presents Q-Q plots for LISA indicators of groundtruth (x-axis) and predicted (y-axis) traffic flows by (a) standard convolutions + grid partition, (b) deformable convolutions + grid partition, (c) standard convolutions + RoI partition, and (d) deformable convolutions + RoI partition. All grid maps are of the size 50×25 . We can observe that grid partition produces many spatial outliers which have less than zero LISA indicators of the groundtruth traffic flows in (a) & (b).

More importantly, we would like to examine and compare standard and deformable convolutions in terms of preserving spatial autocorrelation. To do so, we further draw a diagonal line that passes through the coordinate origin and forms the 45 degree angle with the positive direction of the x-axis in each subfigure, as the reference. Ideally, all points shall fall along the diagonal line, indicating LISA indicators of groundtruth and predicted traffic flows are the same for all grids. By comparing standard and deformable convolutions, we can notice that deformable convolutions can better preserve spatial autocorrelation, as the points in (b) & (d) fall close to the diagonal line, whilst many points in (a) & (c) are far distributed from the diagonal line. Taking the airport as an example, the grid is far away from the diagonal line in (a) & (c), whilst it is just besides the diagonal line in (b) & (d). This indicates that the ablated techniques using

TABLE 5
Performance comparison of different partition shapes (grid vs. RoI) and scales (50×25 vs. 100×50) on TaxiSZ.

Convolution	Metric	50×25		100×50	
		Grid	RoI	Grid	RoI
Standard	RMSE	6.54	6.81	3.09	2.41
	MASE	0.395	0.424	0.354	0.412
Atrous	RMSE	5.79	5.73	2.90	2.27
	MASE	0.477	0.461	0.344	0.422
Deformable	RMSE	5.35	3.09	2.63	2.12
	MASE	0.236	0.322	0.329	0.347

standard convolutions mess up predictions for the airport and neighboring grids, which may mislead users (e.g., taxi drivers) to wrong places when picking up passengers.

4.5 Impacts of Partition Shape and Scale

We further evaluate the performance of *DeFlow-Net* upon various partition schemes. Here we divide the underlying territory into different shapes (grids *vs.* RoIs) and scales (50×25 *vs.* 100×50). We also compare the results with ablated techniques using standard and atrous convolutions. Table 5 presents the experiment results, which reveal some interesting findings.

- First, our proposed *DeFlow-Net* outperforms the ablated techniques in all partition schemes, in terms of both RMSE and MASE. Notice that at partition scale 100×50 , the improvements by *DeFlow-Net* is relatively small than that at scale 50×25 . One possible reason is that at the finer scale, traffic flows are small for most of the grids, making spatial stationary across geographic space. In such case the benefits of deformable convolutions drop.
- Second, finer scale (*i.e.*, 100×50) always produces better results than coarse scale (*i.e.*, 50×25) in terms of RMSE. The results however do not infer that finer scale is better, but simply because RMSE is a unit-dependent metric. In contrast, the unit-independent metric MASE recommends coarse scale 50×25 . Future researches shall take care about the unit dependence issue.
- Last, at the same partition scale, *DeFlow-Net* with RoI partition always produces better results than with grid partition in terms of RMSE, but not of MASE. Through careful investigation, we find the higher MASEs by RoI partition mainly come from some grids at the boundary regions. The rasterization

process assigns some marginal traffic flows to these grids, and eventually cause large MASEs.

5 RELATED WORK

This work focuses on short-term forecasting for traffic flows [30]. We group related work into three categories: *Traffic flow prediction* summarizes conventional and lately deep-learning-based methods for traffic flow prediction; *spatial nonstationarity* discusses spatial nonstationarity of traffic flows, and its impacts on deep traffic flow prediction; and *deformable convolutions* introduces recent developments of deformable convolution networks.

5.1 Traffic Flow Prediction

Traffic flow prediction can be regarded as a classic time-series forecasting problem. As such, many conventional methods for traffic flow prediction are based on time-series models, such as autoregressive integrated moving average (ARIMA) (e.g., [22], [33]) and structural time-series model (STM) [14], which take advantage of repeating occurrences in temporal historical data to fit parametric models. An alternative approach is nonparametric regression, including k -nearest neighbors (k -NN) (e.g., [4], [34]) and Bayesian network (e.g., [28]). Comparison study [27] showed that parametric models generally outperform nonparametric regressions, yet the performance of nonparametric regressions can be significantly improved by larger databases. For instance, a large value of k coupled with larger databases can provide a better set of neighbors in k -NN models, and consequently improve the prediction accuracy.

Nevertheless, the complexity of finding neighbors increases dramatically with larger k values and database sizes. Deep neural networks (DNNs) can suppress the challenge by learning hidden features in traffic flows via dedicated network architectures. As a result, DNNs are being increasingly used for traffic flow prediction. Early attempts with fully connected neural networks [18], [21] achieve superior performances than conventional approaches. Lately, convolution-based neural networks (e.g., [43], [11], [44]) that learns spatial dependence, and graph-based neural networks (e.g., [36], [45], [15], [45]) that naturally fits the road network, have been utilized for predicting traffic flows.

This work focuses on predicting traffic flows in regions, for which convolution-based neural networks are frequently utilized. However, existing convolution-based methods typically adopt standard convolutions with fixed geometric structures to learn spatial dependence across the whole space. The assumption of spatial stationarity is problematic, since a global trend do not reflect the underlying data generating processes [3]. Instead, we employ deformable convolutions that are competent to model the sophisticated spatial nonstationarity in local traffic flows.

5.2 Spatial Nonstationarity

When modeling spatial-temporal dynamics, Anselin emphasized in his influential textbook [2] two intrinsic characteristics of spatial data that need to be taken into account: *spatial dependence* and *spatial nonstationarity* (or spatial heterogeneity). As Tobler's first law of geography [29]

observed, "everything is related to everything else, but near things are more related than distant things", *spatial dependence* refers to a situation where attribute values observed at one spatial unit are dependent on neighboring values at nearby spatial units. In contrast, *spatial nonstationarity* points to the lack of spatial stationarity in attribute values of a particular measure across all spatial units [3].

By far, the literature of convolution-based deep traffic flow prediction concentrates on modeling spatial dependence, whilst little attention has been put on modeling spatial nonstationarity. Yao et al. [37] showed that including regions with weak correlations for a target region can hurt the prediction performance, and designed local CNNs to filter weakly correlated remote regions. Cheng et al. [8] proposed a dynamic spatio-temporal k -nearest neighbor model to capture the heterogeneous spatio-temporal pattern of road traffic. Their work is inspiring but differs with our approach that utilizes deformable convolutions to *automatically* learn spatial nonstationarity from traffic flows. Perhaps most similar to our work is DST-ICRL [11] that combines irregular convolutional residual network with long short term memory network. However, DST-ICRL needs to divide passenger flows of different traffic lines or routes into multiple channels, and utilizes irregular convolution kernels to capture the interpretable high-level dependency in each individual channel. The process is time-consuming and may damage the dependence among spatial units. Instead, our proposed *DeFlow-Net* reserves traffic flows of all spatial units as one single input, being able to learn spatial dependence and nonstationarity simultaneously.

5.3 Deformable Convolution

Convolutional layers that learn abstract feature maps using convolution kernels, are basic components in convolutional neural networks. Standard convolution kernels are defined by fixed shapes of equal width and height (e.g., 3×3 or 5×5), which however may lose some neighboring information as the receptive field of a standard convolution kernel only covers an area with checkerboard patterns [32]. The deficiency may impede certain prediction tasks that feature dynamic spatial correlations, such as semantic segmentation and traffic flow prediction.

Atrous convolution, also known as dilated convolution, inserts holes (i.e., *trous* in French) between pixels to enlarge the field of convolution kernels [7]. A well-known example is DeepLab [6] that employs Atrous Spatial Pyramid Pooling (ASPP) to capture multi-scale objects and context information by placing multiple dilated convolution layers in parallel. Although atrous convolution can enable dense feature extraction, the convolutional kernels are designed to sample the input tensors at symmetric positions, making it difficult to align key points or salient features at arbitrary positions. Therefore, atrous convolutions can still lead to the loss of total information given the discontinuous sampling [35].

To overcome the limitation, Dai et al. [9] proposed deformable convolution as a general form of atrous convolution, by learning sampling offsets dynamically from input tensors. Due to its generalizability, deformable convolution has been successfully applied in many computer vision applications, e.g., semantic segmentation [5], image deblur-

ring [39], and video enhancement [10]. We introduce deformable convolutions for traffic flow prediction, and design *DeFlow-Net* accordingly. Experimental results demonstrate the superior performance of deformable convolutions than standard and atrous convolutions.

6 DISCUSSION AND CONCLUSION

Though being an intrinsic property, the local nonstationary characteristic of traffic flows has been seldom considered in deep traffic flow prediction. This work calls for attention to the impacts of spatial nonstationarity on convolution-based DNN models. We tackle the problem from two perspectives of network inputs and architecture.

First, we show that spatial partition schemes, including both partition shapes and scales (*i.e.*, the MAUP [13], [25]), can affect local nonstationarity across the geographic space. Consequently, prediction performance of convolution-based DNN models are different. Specifically, spatial partition according to perceived RoIs (RoI partition) tends to relax spatial nonstationarity and increase prediction accuracy, in comparison to spatial partition based on the longitude and latitude (grid partition). Besides, finer-grained partition scale (TaxiSZ 100×50) always produces smaller absolute errors than coarse scale (TaxiSZ 50×25), yet the inference is not reliable if we consider unit independent metrics, *e.g.*, MASE adopted in this work. Hence, this work suggests to integrate RoI and movements when preparing network inputs (Sect. 3.1), and choose appropriate partition scale according to practical requirements.

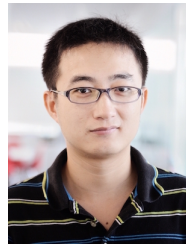
Second, realizing the impacts of spatial nonstationarity, we design *DeFlow-Net* (Sect. 3.2), a deep deformable convolutional residual network that incorporates deformable convolutions to enhance the capability of extracting spatial features. *DeFlow-Net* outperforms existing convolution-based DNN models and ablated techniques, throughout all three real-world datasets. The advancements include both prediction accuracy in terms of RMSE and MASE, and the ability to preserve spatial autocorrelation. The results indicate that deformable convolutions can model both globally spatial dependence and locally spatial nonstationarity. As such, we recommend deformable convolutions, instead of standard convolutions, when constructing the network architecture of convolution-based DNN models.

There are several directions for future research, as follows. First, the DNN models used in this work are treated as ‘black box’, and we apply ‘what-if’ analysis to examine the impacts of spatial nonstationarity on prediction performance. To better understand the working mechanism and improve the model, we would like to open the black box and display the internal states of the DNN models, such as to interpret the hidden unit response to feature selections [26]. Second, this work relies solely on traffic flows for prediction. Studies have shown that incorporating external factors, such as weather [31], [43] and context information [20], can improve the prediction performance. We would also like to redesign the network architecture to fuse these factors. Nevertheless, the heterogeneous data also exhibit independent spatial nonstationarity, bringing in more challenges for network prediction.

REFERENCES

- [1] L. Anselin. Local indicators of spatial association—LISA. *Geographical Analysis*, 27(2):93–115, 1995. 2
- [2] L. Anselin. *Spatial econometrics: methods and models*, volume 4. Springer Science & Business Media, 2013. 9
- [3] C. Brunsdon, A. S. Fotheringham, and M. E. Charlton. Geographically weighted regression: a method for exploring spatial nonstationarity. *Geographical Analysis*, 28(4):281–298, 1996. 1, 9
- [4] H. Chang, Y. Lee, B. Yoon, and S. Baek. Dynamic near-term traffic flow prediction: system-oriented approach based on past experiences. *IET Intelligent Transport Systems*, 6(3):292–305, 2012. 9
- [5] F. Chen, F. Wu, J. Xu, G. Gao, Q. Ge, and X.-Y. Jing. Adaptive deformable convolutional network. *Neurocomputing*, 2020. 2, 9
- [6] L. Chen, G. Papandreou, I. Kokkinos, K. Murphy, and A. L. Yuille. DeepLab: Semantic image segmentation with deep convolutional nets, atrous convolution, and fully connected CRFs. *IEEE Transactions on Pattern Analysis and Machine Intelligence*, 40(4):834–848, 2018. 9
- [7] L.-C. Chen, G. Papandreou, F. Schroff, and H. Adam. Rethinking atrous convolution for semantic image segmentation. *arXiv preprint arXiv:1706.05587*, 2017. 9
- [8] S. Cheng, F. Lu, and P. Peng. Short-term traffic forecasting by mining the non-stationarity of spatiotemporal patterns. *IEEE Transactions on Intelligent Transportation Systems*, 2020. 9
- [9] J. Dai, H. Qi, Y. Xiong, Y. Li, G. Zhang, H. Hu, and Y. Wei. Deformable convolutional networks. In *Proceedings of the IEEE International Conference on Computer Vision*, pages 764–773, 2017. 2, 5, 9
- [10] J. Deng, L. Wang, S. Pu, and C. Zhuo. Spatio-temporal deformable convolution for compressed video quality enhancement. In *Proceedings of the AAAI Conference on Artificial Intelligence*, pages 10696–10703, 2020. 10
- [11] B. Du, H. Peng, S. Wang, M. Z. A. Bhuiyan, L. Wang, Q. Gong, L. Liu, and J. Li. Deep irregular convolutional residual LSTM for urban traffic passenger flows prediction. *IEEE Transactions on Intelligent Transportation Systems*, 21(3):972–985, 2019. 9
- [12] R. C. Geary. The contiguity ratio and statistical mapping. *The Incorporated Statistician*, 5(3):115–141, 1954. 7
- [13] C. E. Gehlke and K. Biehl. Certain effects of grouping upon the size of the correlation coefficient in census tract material. *Journal of the American Statistical Association*, 29(185A):169–170, 1934. 3, 10
- [14] B. Ghosh, B. Basu, and M. O. Mahony. Multivariate short-term traffic flow forecasting using time-series analysis. *IEEE Transactions on Intelligent Transportation Systems*, 10(2):246–254, 2009. 9
- [15] S. Guo, Y. Lin, N. Feng, C. Song, and H. Wan. Attention based spatial-temporal graph convolutional networks for traffic flow forecasting. In *Proceedings of the AAAI Conference on Artificial Intelligence*, volume 33, pages 922–929, 2019. 9
- [16] S. Guo, Y. Lin, S. Li, Z. Chen, and H. Wan. Deep spatial-temporal 3D convolutional neural networks for traffic data forecasting. *IEEE Transactions on Intelligent Transportation Systems*, 20(10):3913–3926, 2019. 3, 6
- [17] K. He, X. Zhang, S. Ren, and J. Sun. Deep residual learning for image recognition. In *Proceedings of the IEEE Conference on Computer Vision and Pattern Recognition*, pages 770–778, 2016. 5
- [18] W. Huang, G. Song, H. Hong, and K. Xie. Deep architecture for traffic flow prediction: deep belief networks with multitask learning. *IEEE Transactions on Intelligent Transportation Systems*, 15(5):2191–2201, 2014. 9
- [19] R. J. Hyndman and A. B. Koehler. Another look at measures of forecast accuracy. *International Journal of Forecasting*, 22(4):679–688, 2006. 7
- [20] Z. Lin, J. Feng, Z. Lu, Y. Li, and D. Jin. DeepSTN+: Context-aware spatial-temporal neural network for crowd flow prediction in metropolis. In *Proceedings of the AAAI Conference on Artificial Intelligence*, volume 33, pages 1020–1027, Jul. 2019. 10
- [21] Y. Lv, Y. Duan, W. Kang, Z. Li, and F. Wang. Traffic flow prediction with big data: A deep learning approach. *IEEE Transactions on Intelligent Transportation Systems*, 16(2):865–873, 2015. 9
- [22] C. K. Moorthy and B. G. Ratcliffe. Short term traffic forecasting using time series methods. *Transportation Planning & Technology*, 12(1):45–56, 1988. 1, 9
- [23] S. Moosavi-Dezfooli, A. Fawzi, O. Fawzi, and P. Frossard. Universal adversarial perturbations. In *Proceedings of the IEEE Conference on Computer Vision and Pattern Recognition*, pages 86–94, 2017. 3
- [24] P. A. Moran. Notes on continuous stochastic phenomena. In *Biometrika*, pages 17–23, 1950. 7

- [25] S. Openshaw. *The Modifiable Areal Unit Problem*. Geo Books, Norwick, UK, 1984. 3, 10
- [26] Q. Shen, Y. Wu, Y. Jiang, W. Zeng, A. K. H. LAU, A. Vianova, and H. Qu. Visual interpretation of recurrent neural network on multi-dimensional time-series forecast. In *Proceedings of IEEE PacificVis*, pages 61–70, 2020. 10
- [27] B. L. Smith, B. M. Williams, and R. Keith Oswald. Comparison of parametric and nonparametric models for traffic flow forecasting. *Transportation Research Part C: Emerging Technologies*, 10(4):303–321, 2002. 9
- [28] S. Sun, C. Zhang, and G. Yu. A bayesian network approach to traffic flow forecasting. *IEEE Transactions on Intelligent Transportation Systems*, 7(1):124–132, 2006. 9
- [29] W. R. Tobler. A computer movie simulating urban growth in the detroit region. *Economic Geography*, 46(sup1):234–240, 1970. 1, 5, 9
- [30] E. I. Vlahogianni, J. C. Golias, and M. G. Karlaftis. Short-term traffic forecasting: Overview of objectives and methods. *Transport Reviews*, 24(5):533–557, 2004. 1, 9
- [31] D. Wang, W. Cao, J. Li, and J. Ye. DeepSD: Supply-demand prediction for online car-hailing services using deep neural networks. In *Proceedings of the IEEE International Conference on Data Engineering*, pages 243–254, April 2017. 10
- [32] P. Wang, P. Chen, Y. Yuan, D. Liu, Z. Huang, X. Hou, and G. Cottrell. Understanding convolution for semantic segmentation. In *Proceedings of the IEEE Winter Conference on Applications of Computer Vision*, pages 1451–1460, 2018. 9
- [33] B. M. Williams, P. K. Durvasula, and D. E. Brown. Urban freeway traffic flow prediction: Application of seasonal autoregressive integrated moving average and exponential smoothing models. *Transportation Research Record*, 1644(1):132–141, 1998. 1, 9
- [34] C.-H. Wu, J.-M. Ho, and D.-T. Lee. Travel-time prediction with support vector regression. *IEEE Transactions on Intelligent Transportation Systems*, 5(4):276–281, 2004. 9
- [35] X. Xu, X. Xiong, J. Wang, and X. Li. Deformable kernel convolutional network for video extreme super-resolution. *arXiv preprint arXiv:2010.00154*, 2020. 9
- [36] S. Yan, Y. Xiong, and D. Lin. Spatial temporal graph convolutional networks for skeleton-based action recognition. In *Proceedings of the AAAI Conference on Artificial Intelligence*, pages 7444 – 7452, 2018. 9
- [37] H. Yao, F. Wu, J. Ke, X. Tang, Y. Jia, S. Lu, P. Gong, J. Ye, and Z. Li. Deep multi-view spatial-temporal network for taxi demand prediction. *arXiv preprint arXiv:1802.08714*, 2018. 3, 9
- [38] J. Yuan, Y. Zheng, and X. Xie. Discovering regions of different functions in a city using human mobility and POIs. In *Proceedings of the SIGKDD Conference on Knowledge Discovery and Data Mining*, pages 186–194. ACM, 2012. 1, 4
- [39] Y. Yuan, W. Su, and D. Ma. Efficient dynamic scene deblurring using spatially variant deconvolution network with optical flow guided training. In *Proceedings of the IEEE Conference on Computer Vision and Pattern Recognition*, pages 3552–3561, 2020. 2, 10
- [40] W. Zeng, C.-W. Fu, S. Müller Arisona, S. Schubiger, R. Burkhard, and K.-L. Ma. Visualizing the relationship between human mobility and points-of-interest. *IEEE Transactions on Intelligent Transportation Systems*, 18(8):2271–2284, 2017. 1, 4
- [41] W. Zeng, C. W. Fu, S. Müller Arisona, A. Erath, and H. Qu. Visualizing waypoints-constrained origin-destination patterns for massive transportation data. *Computer Graphics Forum*, 35(8):95 – 107, 2016. 1
- [42] W. Zeng, C. Lin, J. Lin, J. Jiang, J. Xia, C. Turkay, and W. Chen. Revisiting the modifiable areal unit problem in deep traffic prediction with visual analytics. *IEEE Transactions on Visualization and Computer Graphics*, 2021. 3
- [43] J. Zhang, Y. Zheng, and D. Qi. Deep spatio-temporal residual networks for citywide crowd flows prediction. In *Proceedings of the AAAI Conference on Artificial Intelligence*, pages 1655–1661, 2017. 3, 6, 9, 10
- [44] J. Zhang, Y. Zheng, J. Sun, and D. Qi. Flow prediction in spatio-temporal networks based on multitask deep learning. *IEEE Transactions on Knowledge and Data Engineering*, 32(3):468–478, 2019. 9
- [45] C. Zheng, X. Fan, C. Wang, and J. Qi. GMAN: A graph multi-attention network for traffic prediction. In *Proceedings of the AAAI Conference on Artificial Intelligence*, pages 1234–1241, 2020. 9
- [46] S. Zheng, Y. Song, T. Leung, and I. Goodfellow. Improving the robustness of deep neural networks via stability training. In *Proceedings of the IEEE Conference on Computer Vision and Pattern Recognition*, pages 4480–4488, 2016. 3



Wei Zeng is currently an associate professor at Shenzhen Institutes of Advanced Technology, Chinese Academy of Sciences (CAS). He received his B.E. and Ph.D degree both in computer science from Nanyang Technological University in 2011 and 2015, respectively. Before joining CAS, he worked as a senior researcher at Future Cities Laboratory, ETH Zurich. His research interests include geospatial data analysis and visualization, AR/VR, and urban computing.



Chengqiao Lin is currently a master student in School of Informatics, Xiamen University. His research interests include spatiotemporal data mining, intelligent transportation systems and urban computing.



Kang Liu is currently an associate professor at Shenzhen Institutes of Advanced Technology, Chinese Academy of Sciences. She obtained her Ph.D. degree in Institute of Geographic Sciences and Natural Resources Research (IGSNRR), Chinese Academy of Sciences (CAS) in 2018. Her research interests focus on geospatial data intelligence and urban computing, and application fields of intelligent transportation, public health, and urban planning.



Juncong Lin is currently a full professor in School of Informatics, Xiamen University, leading the Graphics and Virtual Reality Laboratory. He received his B.S. and Ph.D Degree both from Zhejiang University in 2003 and 2008 respectively. Before joining Xiamen University, he has worked in CUHK, NTU as a postdoc researcher. His research interests include data analysis, educational visualization, creativity support tools, and geometry process.



Anthony K. H. Tung is currently a Professor in the Department of Computer Science, National University of Singapore (NUS). He received both his B.Sc. and M.Sc. in computer sciences from the National University of Singapore in 1997 and 1998 respectively. In 2001, he received the Ph.D. in computer sciences from Simon Fraser University (SFU). Dr Anthony Tung main research areas are on searching, mining and visualizing complex data. More recently, he also looks into the creation of innovative big data applications

over the data processing techniques that he had developed over the past 18 years. Anthony is also the deputy director of NUS NCript research center (<https://ncript.comp.nus.edu.sg/>).